



Data-driven control of the turbulent flow past a cylinder

P. Zwintzsch^a, F. Gómez^{a,*}, H.M. Blackburn^{b,*}

^a Aerospace Engineering & Aviation, School of Engineering, RMIT University, Melbourne VIC 3000, Australia

^b Department of Mechanical and Aerospace Engineering, Monash University VIC 3800, Australia



ARTICLE INFO

Article history:

Received 14 October 2018

Received in revised form 5 February 2019

Accepted 4 March 2019

Available online 12 March 2019

Keywords:

Flow control

Resolvent analysis

POD

Cylinder flow

ABSTRACT

A data-driven approach is employed to control vortex shedding on a circular cylinder for Reynolds numbers 100 and 20,000. The methodology used in this study identifies the spatial location of the non-linear forcing which drives the oscillatory wake by performing a Proper Orthogonal Analysis (POD) based on a Singular Value Decomposition (SVD) constructed from a set of data-snapshots of the flow-field. The location containing the highest forcing is then targeted with a passive device to control the flow. It is shown, that for $Re = 100$ a suppression of 15% of the highest forcing is adequate to fully control vortex shedding while for $Re = 20,000$ a suppression of 50% is necessary to inhibit vortex formations. Turbulent flow results are obtained by extending the DNS data-driven methodology to a RANS formulation. Results obtained in this study are in good agreement with previous experimental approaches in controlling vortex shedding on cylinders.

© 2019 Elsevier Ltd. All rights reserved.

1. Introduction

The investigation of wake structures and vortex shedding of flow behind bluff bodies has been the subject of interest for many decades due to their essential significance in the understanding of flow past bluff bodies and practical importance in aerodynamics and hydrodynamics applications (Rashidi et al., 2016). Such applications and others include the flow past suspension bridges, offshore risers (Kwon et al., 2002), underwater pipelines experiencing periodic vibrations due to currents and waves (Zang and Gao, 2014), chimneys and skyscrapers (Rashidi et al., 2016) and bluff bodies on an aircraft such as the landing gear-struts exposed during take-off and landing. Structures exhibiting vortex shedding experience periodic, fluctuating aerodynamic or hydrodynamic loads due to flow separation and vortex formation in the wake. Therefore, suppressing these loads by controlling the unsteady wake flow around bluff structures to reduce unwanted vibrations and acoustic noise leading to structural fatigue has been of great importance for many years (Lu et al., 2016; Vu et al., 2016a). Furthermore, the large body of research conducted on unsteady flow separation and vortex shedding underlines the significance of this phenomenon.

First systematic research on the development of turbulent wake flow from vortex streets was presented by Roshko (1953). Wake development was investigated experimentally behind a circular cylinder at Reynolds numbers (Re) from 40 to 10,000 based on the cylinder diameter and the free-stream velocity. Three distinct Reynolds number ranges have been observed: Stable range between $40 < Re < 150$ in which the shedding frequency and amplitude remains steady. The shedding frequency denoted by the Strouhal number (St) increases steadily within this range. At Reynolds numbers between $150 < Re < 300$, called the transition range, the velocity and shedding frequency shows irregular bursts. These

* Corresponding authors.

E-mail address: fgomezcarrasco@gmail.com (F. Gómez).

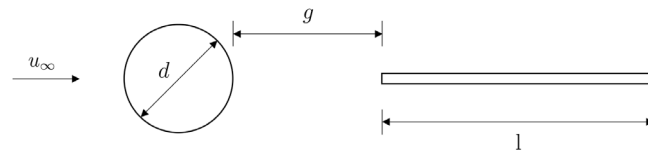


Fig. 1. Schematic arrangement of the splitter plate location and dimension.

bursts tend to become more violent as Re increases. The Strouhal number shows an erratic behaviour in this regime. The development of the unstable two-dimensional wake flow in the transition range was further traced back to the development of highly unstable three-dimensional perturbations which was numerically investigated by Barkley and Henderson (1996). The third Reynolds number regime is called the irregular range from $Re > 300$. The wake behind the cylinder shows irregularities but the predominant shedding frequency can be confidently determined. The Strouhal number is essentially constant in this regime.

The majority of approaches in suppressing vortex shedding behind a cylinder target the suppression of the interaction of the upper and lower shear layers using a passive device located downstream of the cylinder. First experiments were conducted by Roshko using an attached and detached splitter plate located downstream of the cylinder for Reynolds numbers up to 20,000 (Roshko, 1954). The splitter plate used in this research extends to $l = 1.14d$ and was located at downstream locations up to $g/d \leq 6$ where l represents the splitter plate length, d denotes the cylinder diameter and g is the gap distance between the cylinder edge and the splitter plate leading edge and is displayed in Fig. 1.

Vortex shedding was not fully eliminated, but the Strouhal number showed a significant drop of over 30% for $g/d \approx 3.8$ showing an interference with the wake flow. Conclusions drawn from this research stated, that the splitter plate was too short to fully suppress vortex formation. The effect of an attached splitter plate with $l/d \approx 5$ in length also located downstream of the cylinder for $Re = 14,500$ was further investigated in this research. For this experiment the flow was fully controlled by suppressing vortex shedding. Furthermore, with the attached splitter plate the drag coefficient of the cylinder was reduced from 1.1 to 0.7.

The method of suppressing vortex shedding by using splitter plates was adapted by Apelt et al. (1975). Experiments were performed at Reynolds numbers ranging from 10,000 to 50,000 using attached splitter plates with a length range $2 \leq l/d \leq 7$. It was found that vortex shedding is reduced but not eliminated when the splitter plate length exceeds the value of $l/d > 2$. This is to the fact that the flow reattaches at $l/d \approx 4.5$ and forms vortices. Vortex shedding was suppressed for splitter plate lengths of $l/d \geq 5$. A further increase in length has no additional effect on the wake; The drag coefficient remains constant at $C_D = 0.8$ and no vortex shedding from the cylinder was observed.

A study similar to Apelt and West was conducted by M.A.Z Hasan and M.O. Budair for a Reynolds number range of 12,000 to 24,000 for a detached splitter plate (Hasan and Budair, 1994). Experiments were conducted with splitter plate lengths between $0.76 \leq l/d \leq 4.21$ and gap distances of $0 \leq g/d \leq 5.53$. Flow control was not fully achieved but vortex shedding frequency dropped significantly for $l/d = 4.21$ and $g/d = 2$. Similar results were also obtained from Ozono (1999). Vortex shedding was suppressed for $Re = 17,000$ with $l/d = 1$ and $g/d \approx 2$. M.F. Unal and D. Rockwell investigated experimentally the presence of a splitter plate with a wedge-shape leading edge penetrating the wake of a circular cylinder for Reynolds number between $140 < Re < 3600$ (Unal and Rockwell, 1987). It was found, that at low Reynolds numbers e.g. $Re = 142$ the vortex formation instability was eliminated when the splitter plate was placed sufficiently close to the cylinder. For higher Reynolds numbers the vortex formation showed significant variations in the flow structure as mentioned by Roshko (1953). The base pressure and fluctuation level aft the cylinder are lower in the case of higher Reynolds number which result in weaker self-control of the wake. This results in a higher susceptibility of the wake in the presence of a passive flow control device (Unal and Rockwell, 1987). Experiments showed that the flow was fully controlled for $g/d = 3.2$ for $Re = 142$, $g/d \leq 4.5$ for $Re = 785$, $g/d \leq 2.5$ for $Re = 3654$. One of the first numerical simulations investigating flow control on a cylinder using attached and detached splitter plates and control cylinders were performed by Lin and Wu (1994). Simulations were carried out at Reynolds numbers between $80 < Re < 200$ using an artificial compressibility method for solving the incompressible Navier–Stokes equations. The simulation parameters were swept with splitter plate lengths varying between $0.5 \leq l/d \leq 3$ for the attached case and l/d held constant at 2.5 with varying gap lengths between $0.5 \leq g/d \leq 3$ for the detached case. The vortex shedding was controlled for $l/d \geq 2$ for $Re = 100$ with an attached splitter plate and no vortex shedding was observed for $g/d = 2$, $l/d = 2.5$ for $Re = 100$ in case of the detached case. Similar results were obtained numerically by K. Kwon and H. Choi from $80 \leq Re \leq 160$ using an attached splitter plate for flow control around a circular cylinder (Kwon and Choi, 1996). Flow was successfully suppressed when the splitter plate length exceeds the critical length. Kwon and Choi concluded that the critical length increases with increasing Reynolds number considered in this respective Reynolds regime. Vortex shedding was inhibited for $l/d = 3$ for $Re = 100$ and $l/d = 5$ for $Re = 160$. For all simulated Reynolds numbers in this study, no vortex formations were observed for $l/d \geq 5$. This value for the suppression of vortex shedding for various Reynolds numbers is in excellent agreement with experiments conducted by Roshko for $Re = 14,500$ (Roshko, 1954) and Apelt and West for $10,000 \leq Re < 50,000$ (Apelt et al., 1975).

Table 1

Summary of splitter plate locations (non-dimensional length l/d and gap between splitter plate and cylinder g/d) and their respective effectiveness in suppressing vortex formation on a circular cylinder at various Reynolds numbers.

| Source | Research | Splitter Plate Location | | Re | Results |
|--------------------------|--------------|-------------------------|-----------|-------------------|--|
| | | g/d | l/d | | |
| Vu et al. (2016a) | Numerical | No Gap | 1–5 | 60–18 | Fully controlled flow for $l/d = 1.5, 3, 3.5, 4, 4.5$ and 5 for $Re = 80, 100, 120, 140, 160$ and 180 |
| Lin and Wu (1994) | Numerical | No Gap | 0.5–3 | 80–200 | For $g/d = 0$ and $l/d \geq 2$ no vortex shedding for $Re = 100$ for an attached splitter plate For $g/d = 2$ and $l/d = 2.5$ no vortex shedding for $Re = 100$ for a detached splitter plate |
| Mittal (2003) | Numerical | 2.7 | 2 | 100 | Fully controlled flow |
| Kwon and Choi (1996) | Numerical | No Gap | 0–5 | 80–160 | Fully controlled flow for $l/d = 3$ for $Re = 100$ and $l/d = 5$ for $Re = 160$ |
| Serson et al. (2014) | Numerical | 0–3 | 0.5–1 | 100–350 | Not fully controlled, max. 50% reduction in vortex shedding frequency |
| Hwang et al. (2003) | Numerical | 0–5 | 1 | 30–160 | Vortex formation suppressed for $g/d = 2.7$ at $Re = 160$ |
| Unal and Rockwell (1987) | Experimental | 3–15 | 24 | 140–5000 | Flow fully controlled at $g/d = 2.8$ for $Re = 142$, $g/d \leq 5$ for $Re = 785$, $g/d \leq 3$ for $Re = 3654$ |
| Liu et al. (2016) | Experimental | No Gap | 0–1.5 | 2400,3000 | Fully controlled flow for $l/d = 1.125$ for $Re = 2400$ and 3000 |
| Akilli et al. (2005) | Experimental | 0–2 | 1 | 5500 | Vortex shedding elimination for $g/d = 1.75$ |
| Ozono (1999) | Experimental | 0–6 | 1 | $6.7e3$ – $2.5e4$ | Vortex shedding suppressed for $g/d \sim 2$ |
| Hasan and Budair (1994) | Experimental | 0–5.53 | 0.76–4.21 | $1.2e4$ – $2.4e4$ | Minimum of vortex shedding at $g/d = 2$ and $l/d = 4.21$, but not fully controlled |
| Apelt et al. (1975) | Experimental | No Gap | 2–7 | $1e4$ – $5e4$ | Vortex shedding eliminated for $l/d \geq 5$ |
| Roshko (1954) | Experimental | No Gap | 2.7 | 51.14 | Fully controlled flow for $l/d \geq 5$ and no gap Not fully controlled for $g/d = 2.7$ and $l/d = 1.14$ but 30% reduction in vortex shedding frequency |
| Igbalajobi et al. (2013) | Experimental | No Gap | 1 – 7 | $7.4e4$ | Vortex shedding elimination for $l/d \geq 4.5$ |

A detailed but not exhaustive overview was given of the control of vortex shedding in wake of a circular cylinder using attached and detached splitter plates arranged in the symmetry plane of the cylinder and is concluded in Table 1. Two major Reynolds number ranges have been identified serving as a benchmark problem for vortex shedding around circular cylinders: (1) $Re = 100$ and (2) $Re = 20,000$ representing the stable range (1) and irregular range (2) following the nomenclature proposed by Roshko.

Nonetheless, a remarkable amount of research has been dedicated to flow control of vortex shedding around cylinders using alternative approaches. Besides flow control with a splitter plate, many other means and modifications of splitter plates and other passive devices exist, such as porous splitter plates (Ozkan et al., 2017), flexible and hinged splitter plates (Shukla et al., 2009; Sudhakar and Vengadesan, 2012; You et al., 1998), using multiple control rods to control the flow (Gim et al., 2011), dimples on the cylinder surface (Bearman and Harvey, 1993) as well as many other active flow control techniques. A rather comprehensive review of current active and passive methodologies to suppress vortex shedding past cylinders is proposed by Rashidi et al. (2016) and Igbalajobi et al. (2013).

2. Methodology

While the majority of above described methods are based on trial and error approaches, the present study focuses on a different methodology for the design of passive devices to suppress vortex shedding on a circular cylinder. In this paper a data-driven approach of the design of a passive flow control strategy based on previous work from Gómez and Blackburn (2017) is chosen. The data-driven approach operates in an in- and output manner; data-snapshots of the flow-field will be taken from which the spatial location of the non-linear forcing driving the vortex shedding can be derived. Flow control can be achieved by inhibiting the non-linear forcing. This method has been first successfully implemented in the flow control of vortex shedding behind a square cylinder at a low Reynolds number (Gómez and Blackburn, 2017), and later on the control of shear layer oscillations over an open cavity flow (Liu and Gómez, 2019). Underlying framework of this methodology was initially presented by McKeon and Sharma (2010) by treating the non-linear forcing as an unknown and taking advantage of the linear relationship between the non-linear forcing and the velocity field response coupled with a resolvent operator. A singular value decomposition (SVD) of the resolvent is then performed to obtain the forcing shape that drives the most dominant fluctuating velocity field response.

In the following chapters, we will describe and apply the proposed method on the vortex shedding around a circular cylinder. $Re = 100$ and $Re = 20,000$ representing two benchmark cases for the investigation will be chosen. In Section 3, the theoretical framework of the data approach is highlighted. Section 4 covers the numerical setup as well as the mesh dependence study used to obtain the wake fluctuations for both Reynolds numbers. Direct Numerical Simulations (DNS) for the laminar flow case will be performed using the commercial solver ANSYS Fluent 17.2. For the simulation in the irregular flow regime, the $k-\omega$ -SST turbulence model will be employed to close the governing equations. Data snapshots will be taken using an in-house developed User Defined Function (UDF) and will be post-processed using Proper Orthogonal Decomposition (POD). The results of the POD will be presented and discussed in Section 5 and provide the spatial location in which the non-linear forcing excites the oscillatory wake. This will serve as basis for placing a passive device to inhibit vortex shedding.

3. Theoretical framework

Based on the work of Gómez and Blackburn (2017) a brief overview of the underlying theory of the data-driven approach is outlined hereafter. In the present study, incompressible Navier–Stokes Equations (NSE) in conservation form are employed:

$$\nabla \cdot u = 0, \quad (1)$$

$$\partial_t u + u \cdot \nabla u = -\nabla p + Re^{-1} \nabla^2 u \quad (2)$$

where u is the velocity vector expressed in Cartesian coordinates (x, y) , Re is the Reynolds number based on the reference flow velocity and cylinder diameter and p is the modified pressure.

A triple-decomposition of the instantaneous field variables u and p into a temporal mean part and a non-linear coherent and non-coherent component, yields to:

$$u(x, t) = \bar{u}(x) + \tilde{u}(x, t) + u'(x, t), \quad p(x, t) = \bar{p}(x) + \tilde{p}(x, t) + p'(x, t) \quad (3)$$

where $\bar{u}(x)$ denotes the mean value, $\tilde{u}(x, t)$ the coherent contribution of the fluctuating velocity and $u'(x, t)$ denotes the contribution to the non-coherent, stochastic velocity (turbulence) (Hussain and Reynolds, 1970; Speziale, 1987). Furthermore, the coherent fluctuating component and the background turbulence are non-correlated (Hussain and Reynolds, 1970). One can obtain the Reynolds-Averaged Navier–Stokes (RANS) equations by placing the decomposed field variables from (3) in (1) and (2) to yield:

$$\nabla \cdot \bar{u} = 0, \quad (4)$$

$$\partial_t \bar{u} + \bar{u} \cdot \nabla \bar{u} = -\nabla p + Re^{-1} \nabla^2 \bar{u} + f \quad (5)$$

With the Reynolds decomposition an additional term has been introduced, called the Reynolds stress f . Similar to u and p , the Reynolds stress f is composed of the Reynolds stress contributing to the mean flow \bar{f} and the contribution to the coherent non-linear forcing \tilde{f} as well as the non-coherent forcing f' . The stochastic non-coherent forcing f' is obtained via the turbulence model. Hence, the coherent non-linear forcing can be obtained via $\tilde{f} = \tilde{u} \cdot \nabla \bar{u}$. Similarly, the relationship for the fluctuating velocity can be derived

$$\partial_t \tilde{u}(x, t) = \mathcal{L} \tilde{u}(x, t) + \tilde{f}(x, t) \quad (6)$$

\mathcal{L} represents the Jacobian of the NSE and $\tilde{u}(x, t)$ respectively $\tilde{f}(x, t)$ the fluctuating components of the velocity field and non-linear forcing. The linear relationship between the fluctuating forcing and velocity can be obtained by exploiting the linear relationship of the temporal operator ∂_t to attain the resolvent operator \mathcal{R} , coupling forcing and velocity. This yields to

$$\tilde{u}(x, t) = \mathcal{R} * \tilde{f}(x, t) \quad (7)$$

where \mathcal{R} represents the resolvent operator calculated to $\mathcal{R} = (\partial_t - \mathcal{L})^{-1}$. Only the linear relationship between fluctuating velocity and forcing is of interest for the purpose of the data-driven approach. The structure of the resolvent itself is not evaluated in this method. Based on the linear relationship shown in (7), a set of s data snapshots of the velocity and forcing can be taken in the manner of

$$\mathcal{U}(t) = [\tilde{u}(t_1) \tilde{u}(t_2) \tilde{u}(t_3) \cdots \tilde{u}(t_s)] \quad (8)$$

and their corresponding non-linear fluctuating forcing

$$\mathcal{F}(t) = [\tilde{f}(t_1) \tilde{f}(t_2) \tilde{f}(t_3) \cdots \tilde{f}(t_s)] \quad (9)$$

A Proper Orthogonal Decomposition (POD) of rank r of the snapshot matrix \mathcal{U} and \mathcal{F} leads to

$$\mathcal{U}(t) = \sum_{i=1}^r \psi_i^u(x) \sigma_i^u(x) \phi_i^u(t), \quad \mathcal{F}(t) = \sum_{i=1}^r \psi_i^f(x) \sigma_i^f(x) \phi_i^f(t) \quad (10)$$

where $\psi_i^u(x)$ and $\psi_i^f(x)$ represent the spatial POD modes, $\sigma_i^u(x)^2$ and $\sigma_i^f(x)^2$ the average kinetic energy of the i th POD mode and $\phi_i^u(t)$ and $\phi_i^f(t)$ represent the corresponding temporal evolution. In a further step, the snapshot matrix is scaled to ensure that the POD modes yield unit energy under the L_2 norm and that they are orthogonal in time.

Substituting the POD-based models of velocity and forcing in (7) leads to

$$\sum_{i=1}^r \psi_i^u(x) \sigma_i^u(x) \phi_i^u(t) = \mathcal{R} \sum_{i=1}^r \psi_i^f(x) \sigma_i^f(x) \phi_i^f(t). \quad (11)$$

Exploiting the orthonormality in time by multiplying both sides with $\phi_i^u(t)$ and averaging in time leads to

$$\psi_i^u(x) \sigma_i^u = \mathcal{R} \sum_{j=1}^r \psi_j^f(x) \sigma_j^f C_{ij}, \quad (12)$$

where C_{ij} represents the correlation between the temporal evolution of the velocity and forcing POD mode. The elements of this correlation matrix can be written as:

$$C_{ij} = (t_s - t_1)^{-1} \int_{t_1}^{t_s} \phi_j^f(t) \phi_i^u(t) dt \quad (13)$$

and represents which of the j th forcing modes drive the i th velocity mode. If the flow is periodic, or presents a few dominant frequencies, the matrix C_{ij} will be close to sparse.

Finally, the discrete-time-domain discretization of the resolvent operator described in (7) can be obtained by rewriting Eq. (12) as

$$u_i(x) = \mathcal{R} f_i(x). \quad (14)$$

This framework permits the identification of the spatial location of the forcing $f_i(x)$ that excites the most energetic flow structures. Based on that, a passive device such as a splitter plate can be placed in such location to suppress the interaction of the forcing with the flow field. In other words, flow control can be achieved by inhibiting the formation of non-linearity $f_i(x)$. In the following steps, we apply this methodology to the control the vortex shedding behind a circular cylinder for $Re = 100$ and $Re = 20,000$.

4. Numerical setup and validation

4.1. Numerical setup

The two-dimensional flow around the circular cylinder was simulated using the commercial solver ANSYS Fluent 17.2. The NSE were solved using a finite-volume approach. The coupling of pressure and velocity field was solved by the Semi-Implicit Pressure Linked Equation (SIMPLE) approach by using a pressure-based segregated algorithm. For $Re = 100$ a Direct Numerical Simulation (DNS) was carried out. For $Re = 20,000$ closure of the RANS was attained by using the $k - \omega$ turbulence model with the Shear Stress Transport (SST) model. The $k - \omega - SST$ model was chosen due to its low computational cost while maintaining a reasonably precise prediction of the flow separation under adverse pressure gradients (Vu et al., 2016b,a). The convective terms were discretized using a second order upwind scheme. Temporal implicit discretization was performed using a second-order time-integration scheme with a physical time-step size of $\Delta t = 0.008$ s. The governing equations can be obtained from Section 3.

4.2. Computational domain

The computational domain is represented by a rectangular domain extending $-16 \leq y/d \leq 16$ and $-16 \leq x/d \leq 20$ where $x(0, 0)$ corresponds to the cylinder centroid. Periodic boundary conditions are used for the upper and lower wall. A uniform velocity inlet is imposed upstream of the cylinder and a Neumann boundary outlet condition is used downstream of it. The Reynolds number based on the freestream velocity u_∞ and cylinder diameter d was implemented by adapting the kinematic viscosity μ of the fluid where ρ corresponds to the fluid density:

$$Re = \frac{u_\infty \rho d}{\mu} \quad (15)$$

The cylinder wall as well as the passive devices are modelled via a no-slip wall condition. The flow field is discretized using an unstructured grid consisting of triangles with different discretizations for $Re = 100$ with 41,000 cells and $Re = 20,000$ with 58,575 cells. Local refinements are applied in the vicinity of the cylinder and passive device wall as well as in the wake of the cylinder. For the URANS simulation inflation layers on the cylinder surface are implemented to achieve a $y^+ < 1$ to model the viscous sublayer. The computational domain and mesh can be seen in Fig. 2.

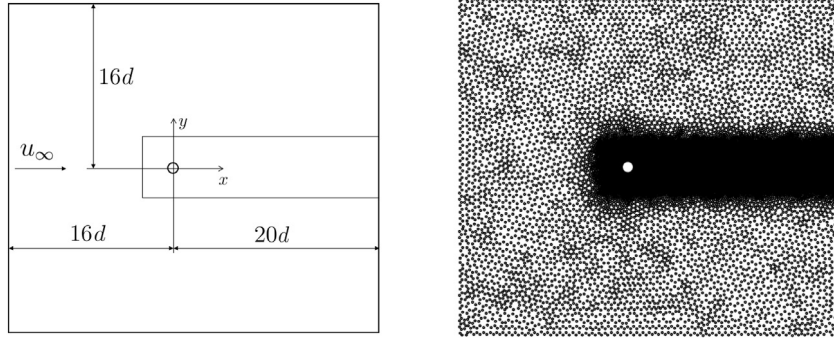


Fig. 2. Computational domain and mesh for cylinder without passive device.

Table 2
Mesh dependence study for different computational meshes for $Re = 100$.

| Mesh | # of cells on cylinder surface | # of total elements | St [-] | Relative error [%] |
|-----------------------------|--------------------------------|---------------------|--------|--------------------|
| A | 200 | 31,700 | 0.1660 | 0.66 |
| B | 300 | 43,000 | 0.1664 | 0.42 |
| C | 450 | 87,500 | 0.1667 | 0.24 |
| D | 500 | 176,000 | 0.1667 | 0.24 |
| Experimental (Roshko, 1953) | | | 0.1671 | – |

4.3. Numerical validation

Numerical results from four different computational meshes were compared to experimental data achieved from previous experiments using the Strouhal number. The Strouhal number is defined as

$$St = \frac{f_s d}{u_\infty} \quad (16)$$

where f_s represents the vortex shedding frequency. The vortex shedding frequency was evaluated for $Re = 100$ and $Re = 20,000$ by the time-series of the lift-force coefficient using Fast Fourier Transformation (FFT). The computational meshes differed in total number of cells as well as the number of elements discretizing the cylinder surface. The results obtained were then compared to the Strouhal number attained experimentally by Roshko (1953). The outcome of the mesh dependence study for $Re = 100$ is listed in Table 2.

Based on Table 2 it can be stated that all meshes provide a fairly precise representation of the Strouhal number. Nonetheless, Mesh B was chosen as computational mesh for $Re = 100$ providing an excellent trade-off with less than 0.5% relative error in terms of vortex shedding frequency compared to the experimental value and computational cost. For the URANS simulations at $Re = 20,000$, a similar study was performed using four different meshes differing in number of elements on the cylinder surface, the wake as well as within the boundary layer to achieve a $y^+ < 1$. A grid with 58,575 cells was chosen with 40 inflation layers located in normal direction of the cylinder surface within a maximum distance of $x_{inflation}/d = 0.1$. A Strouhal number of $St = 0.23$ was obtained for this grid, thus showing a fairly good agreement with experimental data presented by Apelt et al. (1975)

5. Results and discussion

After the simulation has achieved a periodic state, 320 snapshots of the fluctuating velocity $\tilde{u}(t_s)$ and forcing $\tilde{f}(t_s)$ equidistributed over 20 vortex shedding periods have been extracted. The non-linear coherent component of the forcing $\tilde{f}(t_s)$ has been obtained in post-processing by subtracting the mean Reynolds stress \bar{f} from the instantaneous, coherent Reynolds stress $\tilde{f}(t_s)$. A POD has been performed on the snapshot matrices using a randomized Singular-Value Decomposition (SVD). The results of the POD for $Re = 100$ and $Re = 20,000$ are shown hereafter.

The kinetic energy of the first and second velocity POD modes have the highest influence on the wake field by accounting for more than 90% of the total energy (Fig. 3(c)). The mean fluctuating kinetic energy E_k is defined as the sum of each kinetic energy associated to the respective POD mode:

$$E_k = \sum_{i=1}^s \sigma_i^2 \quad (17)$$

The strong influence of these two POD modes on the wake can also be seen in the dominant vortex shedding frequency of $St = 0.1664$ denoted by ϕ_1^u . The doubling of the frequency of the temporal coefficients from one POD pair to the next can

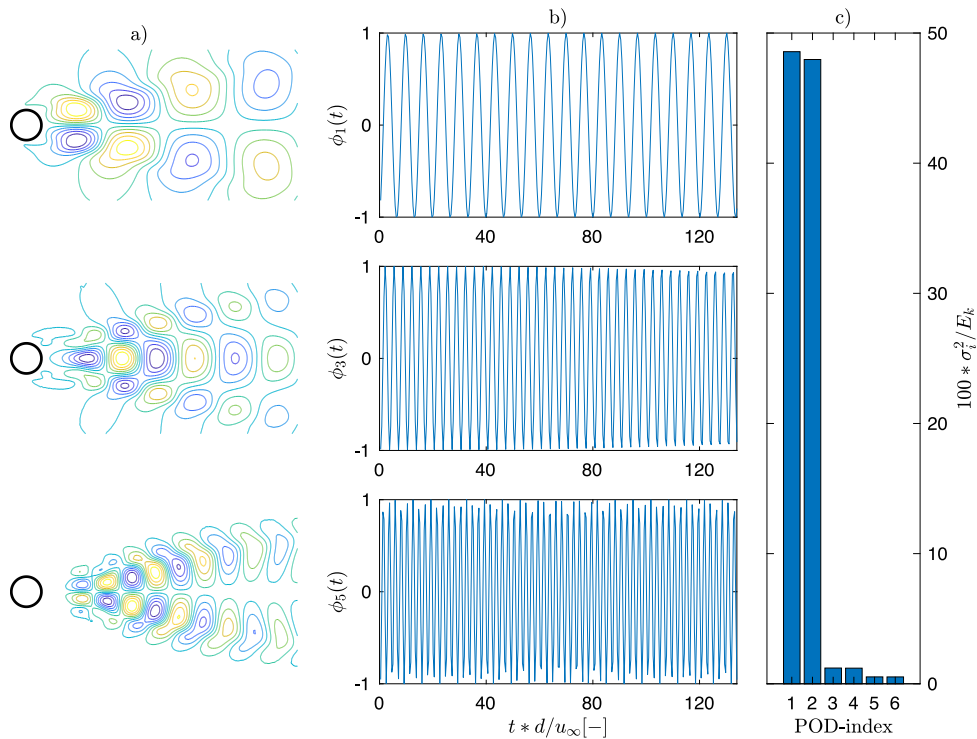


Fig. 3. Fluctuating velocity POD modes for $Re = 100$. Rows from top to bottom show the first, third and fifth velocity POD mode. Column (a) represents the spatial structure $\psi_i^u(x)$ of velocity \tilde{u} , (b) shows the temporal evolution of the coefficient $\phi_i^u(t)$ and (c) represents the kinetic energy associated to each POD mode.

be explained by a decreasing wavelength between POD mode pairs as can be observed in Fig. 2(a). In a similar manner the data snapshots for $Re = 20,000$ have been analysed and summarized in Fig. 4. The fluctuating velocity POD modes show a very similar behaviour compared to $Re = 100$. Analog to $Re = 100$, for $Re = 20,000$ the first two POD modes account for the majority of kinetic energy driving the wake oscillations at a Strouhal number of $St = 0.2372$. The flow pattern of the fluctuating velocity (Fig. 4(a)) shows a higher interference close to the cylinder surface.

In the next step we focus on controlling the wake flow by neutralizing the first and second velocity POD mode for $Re = 100$ and $Re = 20,000$. For that the respective forcing will be identified which excites these two modes. In Fig. 5(a) the kinetic energy associated to each forcing POD mode is displayed. To identify which forcing POD mode drives the dominant velocity POD mode, the correlation matrix C is analysed and can be seen in Fig. 6. The matrix shows, that for $Re = 100$ the third and fourth forcing POD mode drive the oscillatory wake flow (i.e. drive the first two velocity POD modes). For $Re = 20,000$ the fifth and sixth forcing POD mode drive the fluctuating flow field. Furthermore, the fifth forcing POD mode shows a high correlation with the first velocity POD mode and the sixth forcing POD mode show the same correlation with the second velocity POD mode.

The complex conjugate behaviour of the correlation matrix is further displayed in Fig. 5 underlining the periodic behaviour of the vortex shedding. In addition, the correlation matrix shows that $\sum_{i=1}^r C_{ij}^2 \cong 1$, indicating that the chosen POD rank of 6 is sufficient in capturing all the relevant POD modes (Gómez and Blackburn, 2017). The spatial structure of the most energetic i.e. the first two correlated POD modes can be derived via $|\tilde{f}_1 + i\tilde{f}_2|^2$ and represents the area where to forcing is produced and can be seen in Fig. 7.

The spatial structure of the correlated normed POD forcing modes for both Reynolds numbers show a symmetric structure located in the symmetry plane downstream of the cylinder. For $Re = 100$ the structure shows three lobes with the highest correlated forcing situated at $2.5 < x_{Re=100}/d < 4$. The shape of the correlated POD forcing mode correlates very well with the forcing shape found by Gómez and Blackburn. For $Re = 20,000$ the structure shows a single lobe situated closer to the cylinder and more stretched in the downstream direction of the wake, forming two concentrated locations with correlated POD forcing bigger than 80%. The highest correlated POD forcing is situated between $1.5 < x_{Re=20,000}/d < 4.5$.

Based on the spatial structure we target the area containing the highest correlated forcing with a passive device in a shape of a flat plate and an ellipse. The percentage of forcing which needs to be suppressed to control the flow was evaluated in an iterative approach using 15%, 30% and 50% suppression of the highest correlated POD forcing. The higher the percentage of suppression the bigger are the dimensions of the passive device. The downstream-location of the device

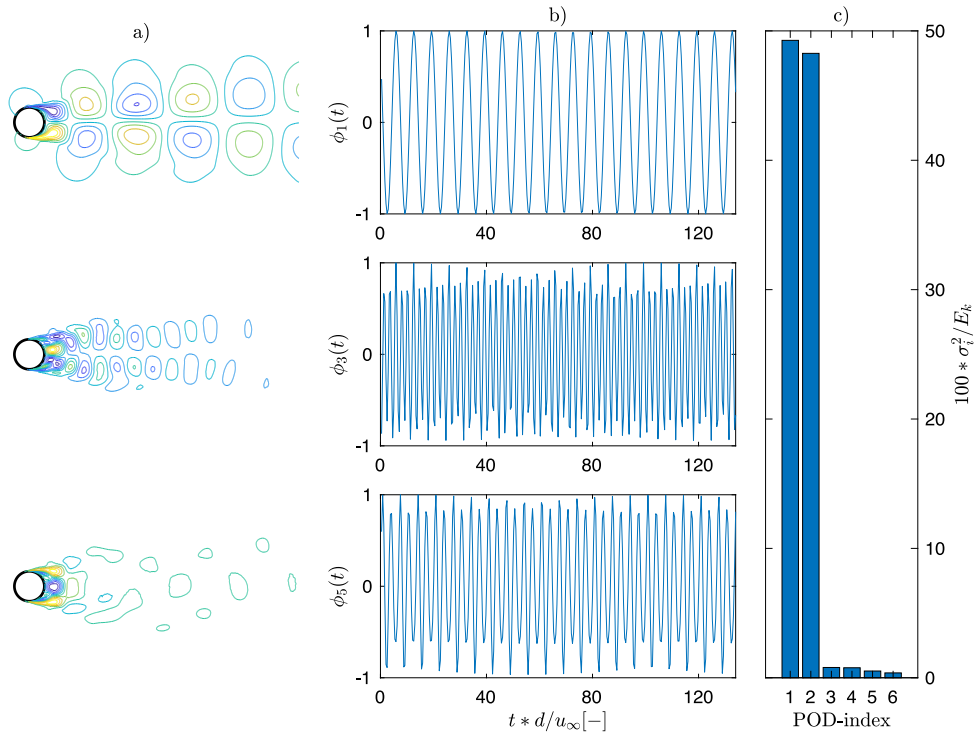


Fig. 4. Fluctuating velocity POD modes for $Re = 20,000$. Rows from top to bottom show the first, third and fifth velocity POD mode. Column (a) represents the spatial structure $\psi_i^u(x)$ of velocity \tilde{u} , (b) shows the temporal evolution of the coefficient $\phi_i^u(t)$ and (c) represents the kinetic energy associated to each POD mode.

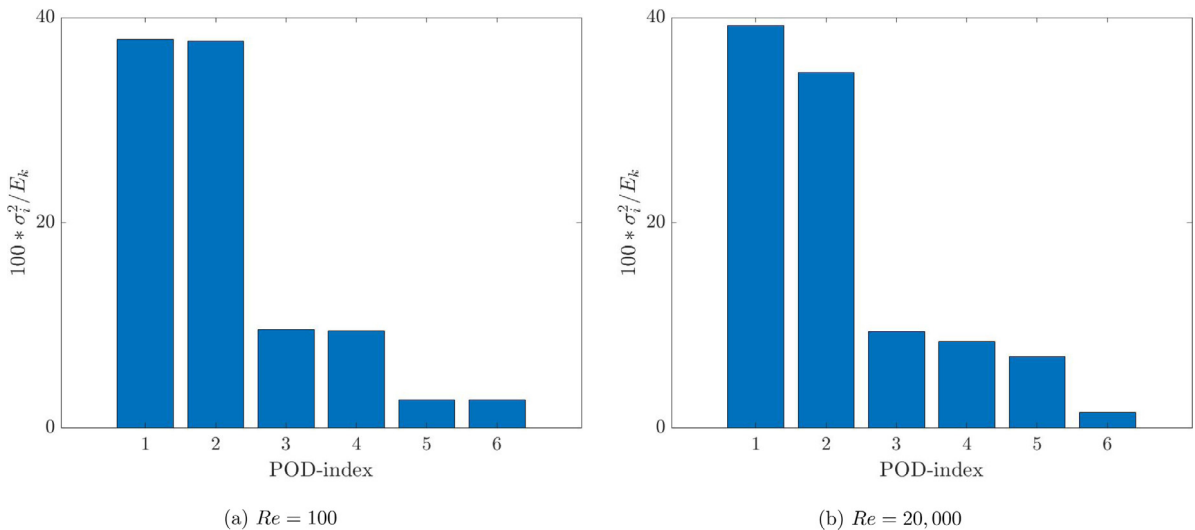


Fig. 5. Percentage of kinetic energy associated to each forcing POD mode ψ_i^f for $Re = 100$ (left) and $Re = 20,000$ (right).

was held constant between splitter plate and ellipse per suppression-case and Reynolds number. In the case of an ellipse the length of the major and minor axes was adapted. For the splitter plate the length was modified and the thickness t was held constant at $t/d = 0.1$ to retain a certain slenderness of the splitter plate. The resulting dimensions from suppressing 15%, 30% and 50% of the correlated POD forcing is summarized in Table 3 and visualized in Figs. 8(a) and 8(b) using an ellipse as passive device.

The effect of the passive device on the wake flow is presented and discussed hereafter. For $Re = 100$ it has shown that 15% suppression of correlated POD forcing is sufficient to fully control the wake flow as can be seen in Fig. 9. For

$$C_{Re=100} \simeq \begin{pmatrix} \epsilon & \epsilon & -0.725 & -0.688 & \epsilon & \epsilon \\ \epsilon & \epsilon & 0.688 & -0.725 & \epsilon & \epsilon \\ -0.960 & -0.278 & \epsilon & \epsilon & \epsilon & \epsilon \\ 0.278 & 0.960 & \epsilon & \epsilon & \epsilon & \epsilon \\ \epsilon & \epsilon & \epsilon & \epsilon & 0.921 & 0.390 \\ \epsilon & \epsilon & \epsilon & \epsilon & -0.390 & 0.921 \end{pmatrix}$$

$$C_{Re=20,000} \simeq \begin{pmatrix} \epsilon & \epsilon & -0.119 & -0.118 & 0.802 & 0.475 \\ \epsilon & \epsilon & -0.129 & \epsilon & 0.495 & -0.853 \\ \epsilon & 0.939 & \epsilon & \epsilon & \epsilon & -0.113 \\ -0.980 & \epsilon & \epsilon & \epsilon & \epsilon & \epsilon \\ 0.194 & -0.325 & \epsilon & \epsilon & -0.233 & -0.119 \\ \epsilon & \epsilon & -0.815 & -0.542 & -0.183 & \epsilon \end{pmatrix}$$

Fig. 6. Structure of the correlation matrix for $Re = 100$ (top) and $Re = 20,000$ (bottom). The rows represent the velocity POD modes, the columns the forcing POD modes. For $Re = 100$ the third and fourth forcing POD mode drive the vortex flow i.e. the first two velocity POD modes. For $Re = 20,000$ the fifth and sixth drive the vortex flow. All columns satisfy that $\sum_{j=1}^r C_{ij}^2 \simeq 1$. ϵ represents elements $O(10^{-3})$.

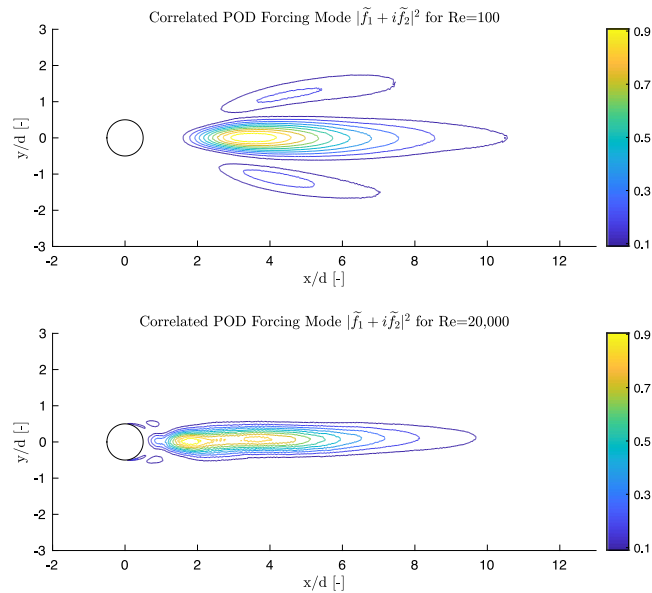


Fig. 7. Structure of the correlated POD forcing mode for $Re = 100$ (top) and $Re = 20,000$ (bottom).

Table 3

Overview of splitter plate and ellipse dimensions for various suppression percentages of correlated POD forcing modes for $Re = 100$ and $Re = 20,000$.

| Suppression [%] | Dimensions for $Re = 100$ | | Dimensions for $Re = 20,000$ | |
|-----------------|---------------------------|---|------------------------------|---|
| | Splitter plate | Ellipse | Splitter plate | Ellipse |
| 15 | $2.78 < x/d < 4.41$ | $2.78 < x/d < 4.41$ $-0.16 < y/d < 0.16$ | $1.53 < x/d < 3.52$ | $1.53 < x/d < 3.52$ $-0.13 < y/d < 0.13$ |
| 30 | $2.54 < x/d < 5.08$ | $2.54 < x/d < 5.08$ $-0.24 < y/d < 0.24$ | $1.42 < x/d < 4.76$ | $1.42 < x/d < 4.76$ $-0.22 < y/d < 0.22$ |
| 50 | $2.27 < x/d < 5.93$ | $2.27 < x/d < 5.93$ $-0.33 < y/d < 0.33$ | $1.24 < x/d < 5.70$ | $1.24 < x/d < 5.70$ $-0.32 < y/d < 0.32$ |

this setup, the leading edge of the passive device was located at $x/d = 2.78$ downstream of the cylinder centroid, with an overall length of $l/d = 1.63$. In the absence of the device the flow exhibits strong vortex shedding. However, in the presence of the passive device vortex shedding is completely eliminated thus leading to a diminishing of the amplitude fluctuations of the stream-wise velocity at $x_1(10, 1.7)$ and lift coefficient.

The spatial location of the passive device needed to control the wake flow correlates very well with previous researches outlined in the literature review. The downstream location of the highest correlated POD forcing with $x/d \geq 2.7$ indicates why vortex shedding cannot be suppressed when the passive device is located too close in the vicinity of the cylinder

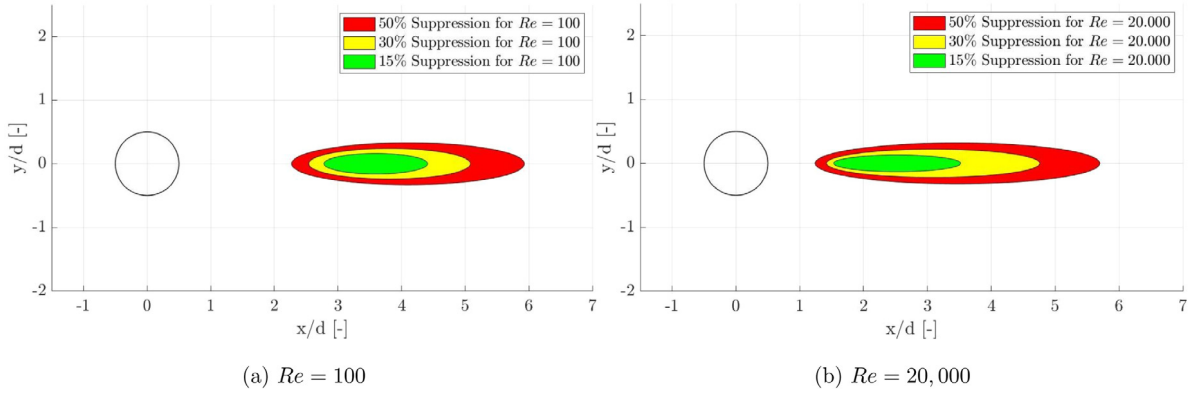


Fig. 8. Comparison of ellipse dimensions used for flow control for $Re = 100$ (left) and $Re = 20,000$ (right) based on Table 3.

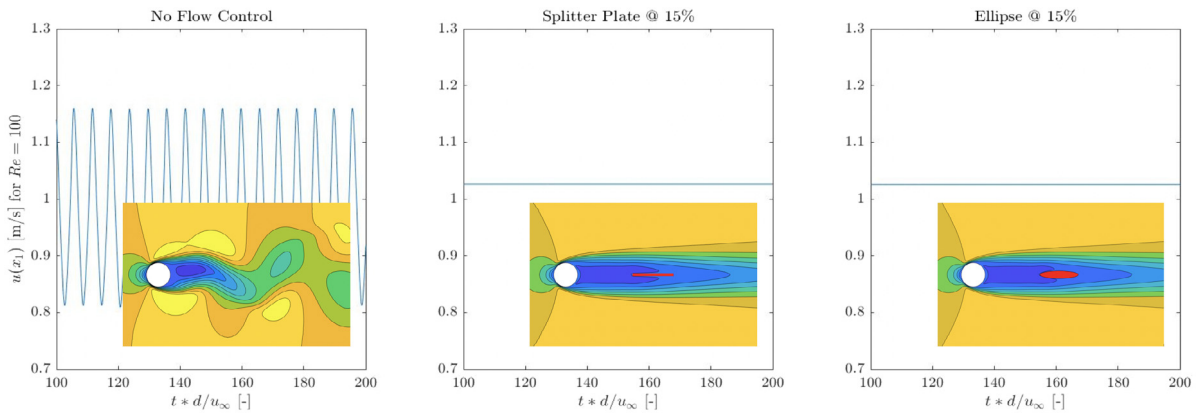


Fig. 9. Influence of the splitter plate and ellipse on the wake for 15% suppression for $Re = 100$. The upper row shows the streamwise velocity component u at $(10, 1.7)$ with no flow control (left), splitter plate (middle) and ellipse (right). The lower row shows the u -velocity contour plot for the wake flow at $t = 100$ s with no flow control, splitter plate and ellipse.

and/or the length does not extend beyond the point of the highest correlated POD forcing. In that case the forcing that drives the wake will be generated further downstream, thus the passive device has no effect on the vortex shedding. This also explains, why vortex shedding can be suppressed for attached splitter plate lengths which extends beyond $l/d \geq 5$ for $Re = 100$ thus suppressing shear layer interaction.

For $Re = 20,000$, the flow field exhibits strong vortex shedding similar to $Re = 100$ in the absence of passive devices. A suppression of 50% has proven to be successful in controlling vortex shedding. For that, the passive devices extend to $l/d = 4.46$ in length and are situated at $x/d = 1.24$ m based on the cylinder centroid and the leading edge of the passive device. For 15% and 30% suppression, vortex shedding could not be reduced. For 50% suppression the lift coefficient fluctuations diminish and the wake field becomes steady as can be seen in Fig. 10. This phenomenon can be traced back to the stretched nature of the spatial structure of the correlated POD forcing mode from Fig. 7. Regarding previous advances in the flow control of cylinders at $Re = 20,000$ it can be stated, that flow control cannot be achieved for splitter plate dimensions $l/d \leq 5$. This value corresponds to a suppression of $\sim 50\%$ which in this research was also found to be a minimal required length ratio for flow control.

6. Conclusion

In this paper, the data-driven approach proposed by Gómez and Blackburn (2017) has been used in the design of a passive device to control vortex shedding on a circular cylinder at Reynolds numbers 100 and 20,000. While there has already been a tremendous amount of research dedicated to this based on a trial and error approach, the present data-driven methodology directly determines the spatial location of the Reynolds stresses that drive the wake flow oscillations after obtaining a set of data snapshots of the flow field. A splitter plate and ellipse arranged downstream of a circular cylinder serve as passive devices targeting the spatial location to suppress vortex shedding. It has been shown, that for $Re = 100$ a suppression of 15% of the highest correlated forcing is enough to fully control vortex formations. In this case,

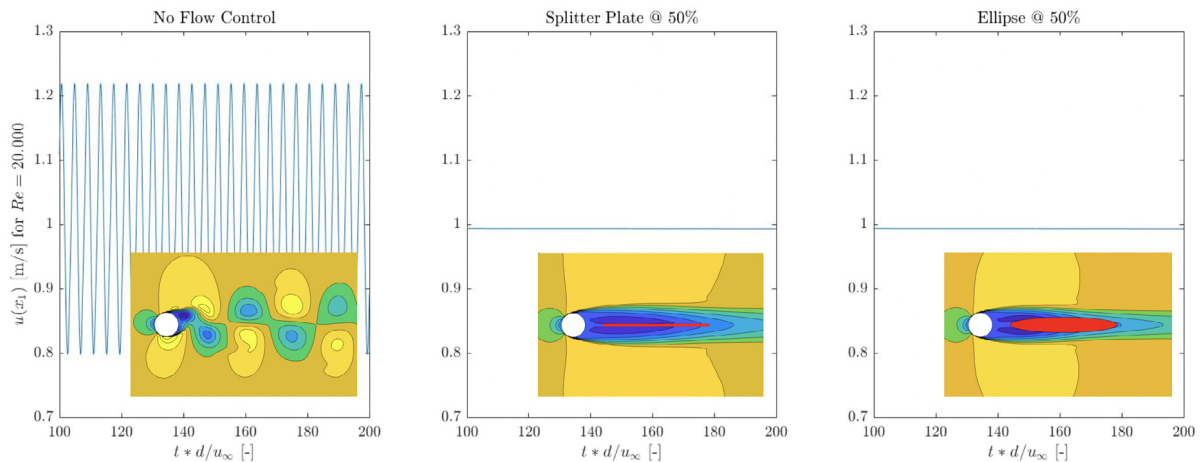


Fig. 10. Influence of the splitter plate and ellipse on the wake for 50% suppression for $Re = 20,000$. The upper row shows the stream-wise velocity component u at $(10, 1.7)$ with no flow control (left), splitter plate (middle) and ellipse (right). The lower row shows the u -velocity contour plot for the wake flow at $t = 100$ s with no flow control, splitter plate and ellipse.

the passive device has a length of $l/d = 1.6$, located at $x/d = 2.8$ downstream of the cylinder. For $Re = 20,000$ a high suppression of 50% is needed to fully control vortex formations. Suppression below 50% had no influence on the wake field. This has been traced back the stretched nature of the spatial structure of the correlated forcing, extending beyond $l/d = 5$ in length downstream of the cylinder whereas the spatial formation for $Re = 100$ shows a much more spatially condensed structure. Both results are in excellent agreement with previous attempts in controlling vortex formation on a circular cylinder. It has to be noted, that although the passive devices used in the current study do not provide the aerodynamically best shape in controlling vortices. The current study, however, can be rated as additional proof of the proposed data-driven methodology in the design of flow control. Furthermore, it extends the methodology proposed by Gómez and Blackburn by demonstrating that unsteady, incompressible RANS simulations can also be evaluated with this methodology. This opens up the ability to evaluate complex aerodynamic phenomena without accounting for the extensive computational costs of DNS.

References

- Akilli, H., Sahin, B., Tumen, N.F., 2005. Suppression of vortex shedding of circular cylinder in shallow water by a splitter plate. *Flow Meas. Instrum.* 16 (4), 211–219.
- Apelt, C.J., West, G.S., Szewczyk, A.A., 1975. The effects of wake splitter plates on the flow past a circular cylinder in the range $1e4 < Re < 5e4$. part2. *J. Fluid Mech.* 71 (1), 145–160.
- Barkley, D., Henderson, R.D., 1996. Floquet stability analysis of the periodic wake of a circular cylinder. *J. Fluid Mech.* 322, 215–241.
- Bearman, P.W., Harvey, J.K., 1993. Control of circular cylinder flow by the use of dimples. *AIAA J.* 31 (10), 1753–1756.
- Gim, O.S., Kim, S.H., Lee, G.W., 2011. Flow control behind a circular cylinder by control rods in uniform stream. *Ocean Eng.* 38 (17–18), 2171–2184.
- Gómez, F., Blackburn, H.M., 2017. Data-driven approach to design of passive flow control strategies. *Phys. Rev. Fluids* 2 (2), 1–8.
- Hasan, M.A.Z., Budair, M.O., 1994. Role of splitter plates in modifying cylinder wake flows. *AIAA J.* 32 (10), 1992–1998.
- Hussain, A.K.M.F., Reynolds, W.C., 1970. The mechanics of an organized wave in turbulent shear flow. *J. Fluid Mech.* 41 (2), 241–258.
- Hwang, J.Y., Yang, K.S., Sun, S.H., 2003. Reduction of flow-induced forces on a circular cylinder using a detached splitter plate. *Phys. Fluids* 15 (8), 2433–2436.
- Igbalajobi, A., McClean, J.F., Sumner, D., Bergstrom, D.J., 2013. The effect of a wake-mounted splitter plate on the flow around a surface-mounted finite-height circular cylinder. *J. Fluids Struct.* 37, 185–200.
- Kwon, S.H., Cho, J.W., Park, J.S., Choi, H.S., 2002. The effects of drag reduction by ribbons attached to cylindrical pipes. *Ocean Eng.* 29 (15), 1945–1958.
- Kwon, K., Choi, H., 1996. Control of laminar vortex shedding behind a circular cylinder using splitter plates. *Phys. Fluids* 8 (2), 479–486.
- Lin, S.-Y., Wu, T.-M., 1994. Flow control simulations around a circular cylinder by a finite volume scheme. *Numer. Heat Transfer A* 26 (3), 301–319.
- Liu, K., Deng, J., Mei, M., 2016. Experimental study on the confined flow over a circular cylinder with a splitter plate. *Flow Meas. Instrum.* 51, 95–104.
- Liu, Q., Gómez, F., 2019. Role of trailing-edge geometry in open cavity flow control. *AIAA J.* 57 (2), 876–878.
- Lu, L., Guo, X.L., Tang, G.Q., Liu, M.M., Chen, C.Q., Xie, Z.H., 2016. Numerical investigation of flow-induced rotary oscillation of circular cylinder with rigid splitter plate. *Phys. Fluids* 28 (9).
- McKeon, B.J., Sharma, A.S., 2010. A critical-layer framework for turbulent pipe flow. *J. Fluid Mech.* 658, 336–382.
- Mittal, S., 2003. Effect of a “slip” splitter plate on vortex shedding from a cylinder. *Phys. Fluids* 15 (3), 817–820.
- Ozkan, G.M., Firat, E., Akilli, H., 2017. Passive flow control in the near wake of a circular cylinder using attached permeable and inclined short plates. *Ocean Eng.* 134 (February), 35–49.
- Ozono, S., 1999. Flow control of vortex shedding by a short splitter plate asymmetrically arranged downstream of a cylinder. *Phys. Fluids* 11 (10), 2928–2934.
- Rashidi, S., Hayatdavoodi, M., Esfahani, J.A., 2016. Vortex shedding suppression and wake control: A review. *Ocean Eng.* 126, 57–80.
- Roshko, A., 1953. On the Development of Turbulent Wakes from Vortex Streets. Technical Report, National Advisory Committee for Aeronautics, Washington, DC, United States, pp. 1–78.
- Roshko, A., 1954. On the wake and drag of bluff bodies. *J. Aeronaut. Sci.* 22 (2), 124–132.

- Serson, D., Meneghini, J., Carmo, B.S., Volpe, E.V., Gioria, R.S., 2014. Wake transition in the flow around a circular cylinder with a splitter plate. *J. Fluid Mech.* 755 (5), 582–602.
- Shukla, S., Govardhan, R.N., Arakeri, J.H., 2009. Flow over a cylinder with a hinged-splitter plate. *J. Fluids Struct.* 25 (4), 713–720.
- Speziale, C.G., 1987. On the decomposition of turbulent flow fields for the analysis of coherent structures. *Acta Mech.* 70, 243–250.
- Sudhakar, Y., Vengadesan, S., 2012. Vortex shedding characteristics of a circular cylinder with an oscillating wake splitter plate. *Comput. & Fluids* 53 (1), 40–52.
- Unal, M., Rockwell, D., 1987. On vortex formation from a cylinder. *J. Fluid Mech.* 190, 513–529.
- Vu, H.C., Ahn, J., Hwang, J.H., 2016a. Numerical investigation of flow around circular cylinder with splitter plate. *KSCE J. Civ. Eng.* 20 (6), 2559–2568.
- Vu, H.C., Ahn, J., Hwang, J.H., 2016b. Numerical simulation of flow past two circular cylinders in tandem and side-by-side arrangement at low reynolds numbers. *J. Civ. Eng.* 20, 1594–1604.
- You, D., Choi, H., Choi, M.-R., Kang, S.-H., 1998. Control of flow-induced noise behind a circular cylinder using splitter plates. *AIAA J.* 36 (11), 1961–1967.
- Zang, Z.P., Gao, F.P., 2014. Steady current induced vibration of near-bed piggyback pipelines: Configuration effects on VIV suppression. *Appl. Ocean Res.* 46, 62–69.